metals

MDPI

Article

Investigation of Microstructure and Mechanical Properties of the Repaired Precipitation-Strengthened Ni-Based Superalloy via Laser Melting Deposition

Wengao Yan [1,2,3,4], Beirao Xue [1,2,3,4], Jinjun Li [1,2,3], Minghuang Zhao [1,2,3] and Xiangde Bian [1,2,3,*]

[1] Advanced Gas Turbine Laboratory, Institute of Engineering Thermophysics, Chinese Academy of Sciences, Beijing 100190, China; 18674378306@163.com (W.Y.); xuebeirao@iet.cn (B.X.); lijinjun@iet.cn (J.L.); zhaominghuang@iet.cn (M.Z.)
[2] Key Laboratory of Advanced Energy and Power, Institute of Engineering Thermophysics, Chinese Academy of Sciences, Beijing 100190, China
[3] National Key Laboratory of Science and Technology on Advanced Light-duty Gas-Turbine, Chinese Academy of Sciences, Beijing 100190, China
[4] University of Chinese Academy of Sciences, Beijing 100049, China
* Correspondence: bianxiangde@iet.cn; Tel.: +86-156-5079-8558

Abstract: In this study, a typical γ′ phase precipitation-strengthened Ni-based superalloy DZ411 was repaired using an LMD-based repairing technique with an IN738LC superalloy, and crack-free samples were acquired. The mechanical properties and microstructure of different areas inside the repair sample were investigated, including the IN738LC deposit, the DZ411 substrate, and the interface between these two parts. The differences in mechanical properties between different areas were explained via analyzing fractography and KAM maps. It was found that the coarse carbides of the DZ411 substrate might lead to rapid cracking of grain boundaries, resulting in the worst mechanical properties of the DZ411 substrate. The IN738LC deposit demonstrated significantly superior mechanical properties in comparison to the DZ411 substrate. Its tensile strength exceeded that of the substrate by over 250 MPa, while its relative elongation after fracture was twice as great as that of the substrate. The excellent mechanical properties of the IN738LC deposit could be attributed to its fine microstructure, which resisted rapid cracking and generated a large number of GNDs during the plastic deformation process. For the interface between the deposit and substrate, although its hardness before the tensile test was low, it could also generate many GNDs during the plastic deformation process, hence exhibiting commendable mechanical properties. The research results show that using an LMD-based repairing technique with IN738LC superalloy to repair γ′ phase precipitation-strengthened Ni-based superalloy DZ411 is a feasible solution.

Keywords: Ni-based superalloy; repair; microstructure; tensile behavior; work hardening

Citation: Yan, W.; Xue, B.; Li, J.; Zhao, M.; Bian, X. Investigation of Microstructure and Mechanical Properties of the Repaired Precipitation-Strengthened Ni-Based Superalloy via Laser Melting Deposition. *Metals* **2023**, *13*, 1957. https://doi.org/10.3390/met13121957

Academic Editor: Abdollah Saboori

Received: 18 October 2023
Revised: 25 November 2023
Accepted: 27 November 2023
Published: 30 November 2023

1. Introduction

Precipitation-strengthened Ni-based superalloys are frequently used as turbine blade material in gas turbines, which operate in high-temperature, high-pressure, and high-speed environments, thereby making them susceptible to wear, cracking, and other damages [1–3]. The laser melting deposition (LMD) technique is an advanced technique that utilizes laser energy to melt metal powder, enabling the gradual formation of components via layer-by-layer stacking [4,5]. This technique provides the advantages of low heat input and high material availability, as well as the ability to ignore the complexity of structure, which makes it well-suited for repairing damaged blades [6,7].

However, achieving the successful reparation of precipitation-strengthened Ni-based superalloys is a considerable challenge. The primary factor contributing to this challenge is the poor weldability of the most precipitation-strengthened Ni-based superalloys, which

leads to solidification cracks [8,9], liquation cracking [10], or some other defects [11] in the alloys during the repair procedure. Researchers have tried many methods to reduce the defect sensitivity of precipitation-strengthened Ni-based superalloys during LMD processing, including heating the substrate [10,12] and reducing heat input [13,14]. Despite extensive research efforts, the manufacturing of large-sized precipitation-strengthened Ni-based superalloys utilizing LMD remains difficult primarily because of the significant residual thermal stress inherent in the LMD process [14,15].

Due to the size limitation caused by residual thermal stress, there are only a few investigations on the mechanical properties of precipitation-strengthened Ni-based superalloys repaired or directly manufactured by LMD [16–18]. Xu et al. [16] manufactured the IN738LC superalloy using LMD, which had higher tensile strength compared with the as-cast IN738LC superalloy. Yu et al. [17] added pure Hf powder during the manufacture of IN738LC superalloy by selective laser melting, which successfully inhibited cracks and improved the mechanical properties of the alloy. Ci et al. [18] repaired DD32 single-crystal superalloy and investigated the relationship between the tensile behavior of the repaired DD32 superalloy and its microstructure. Within these small amounts of existing research, the mechanical properties of the interface between the deposit and substrate were frequently not investigated. For repaired superalloys, the mechanical properties of the interface are also important.

The heterogeneous interface often exhibits considerable compositional and microstructural gradients, resulting in distinctive mechanical properties. Fang et al. [19] designed a dual heterostructure brass that overcame the strength–ductility trade-off and possessed a superior combination of strength and ductility. This comprehensive strengthening effect was attributed to the generation of geometrically necessary dislocations (GNDs) at the heterogeneous interface during plastic deformation [20]. Tan et al. [21] also found that the gradient microstructures in additive-manufactured Ti–6Al–4V could enhance elongation by suppressing strain localization. However, the heterogeneous interface may not always strengthen the alloys. For example, during the melting joining process of two alloys with different compositions, brittle intermetallic compounds might be generated at the interface position, which reduces the interface performance and even induces cracks [22]. Therefore, it is necessary to investigate the mechanical properties of the interface of the repaired superalloy.

In this investigation, we repaired the DZ411 superalloy via LMD with IN738LC superalloy as the filler material, and some crack-free samples were obtained. The mechanical properties of the deposit, the substrate, and the interface between them were next measured, and an investigation was conducted to figure out the factors contributing to the variations in their mechanical properties.

2. Material and Methods

2.1. Materials

DZ411 superalloy is a typical γ' phase precipitation-strengthened Ni-based superalloy that is extensively utilized in turbine blades [23]. This alloy is also susceptible to damage, such as cracks, but due to its high Al and Ti content, it is difficult to use this alloy to repair itself directly [24]. The LMD technique utilized for the IN738LC superalloy has reached a considerable level of development [16,17]. In addition, the chemical composition and physico-thermal properties [25] of IN738LC superalloys are very similar to those of DZ411 superalloys, as shown in Tables 1 and 2. Therefore, it is a feasible method to repair the DZ411 superalloy by using the IN738LC superalloy as the filling material.

Table 1. Chemical composition of IN-738 superalloy and DZ411 superalloy.

Alloy	Ni	Cr	Co	W	Mo	Ti	Al	Nb	Ta	C	Si
IN738LC	bal	16.07	8.6	2.56	1.83	3.36	3.48	0.83	1.82	0.12	0.05
DZ411	bal	13.78	9.64	3.98	1.40	5.06	3.22	–	2.82	0.10	0.012

Table 2. Physico-thermal properties of IN-738 superalloy and DZ411 superalloy [25].

Alloy	Heat Conductivity [W/(m·°C), 1000 °C]	Specific Heat Capacity [J/(kg·°C), 1000 °C]	Thermal Expansivity [10^6 °C^{-1}), 20–1000 °C]
IN738LC	22.1	582	16.1
DZ411	22.5	575	15.9

2.2. Repair Process

The schematic diagram of the repair procedure is shown in Figure 1a. In this study, a carbon dioxide laser CP4000 was employed as a heat source. Although the heat input of the LMD to the substrate was relatively low, a pulsed laser was employed as the heat source to further minimize the heat input and limit the tendency of the sample to crack during the repair process [7]. The specific laser parameters were as follows: a power of 2000 W, a laser spot diameter of 2 mm, a laser spot interval of 0.7 mm, a pulse width of 0.16 s, and a pulse interval of 0.3 s.

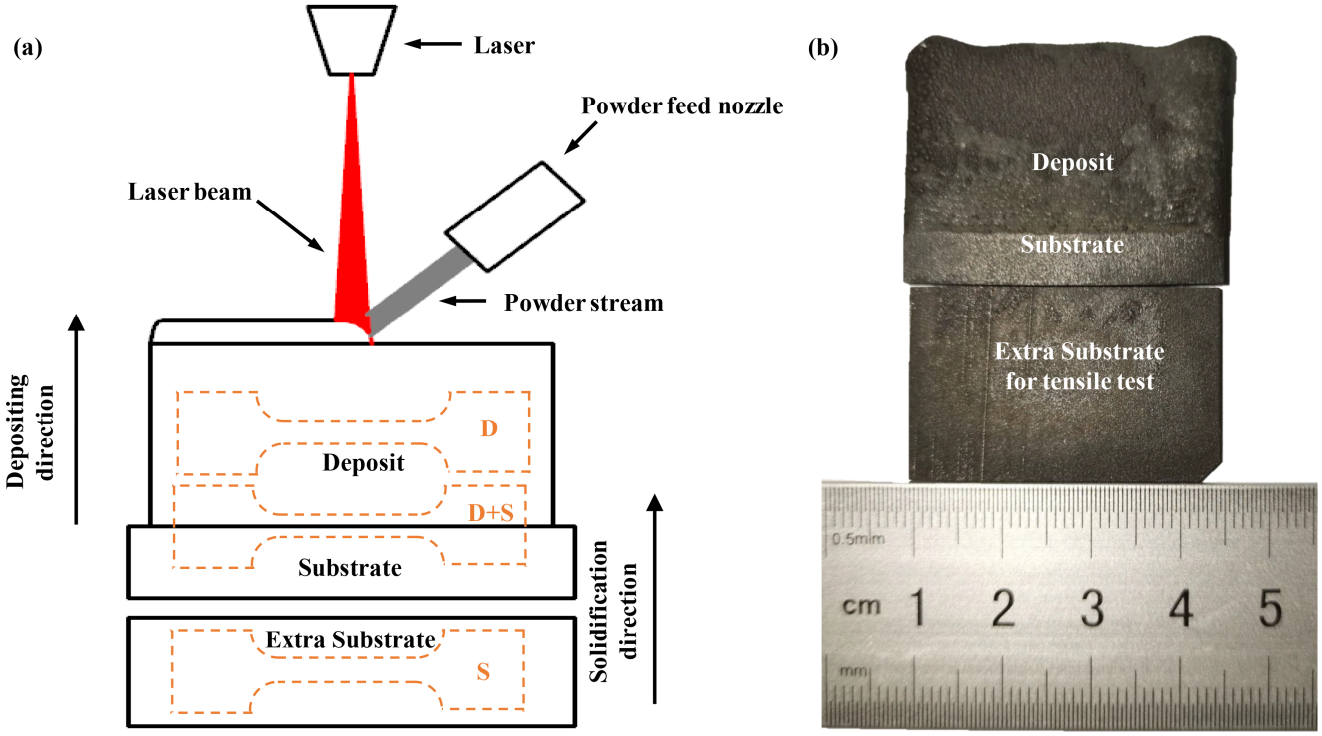

Figure 1. (**a**) Schematic diagram of the repairing process and the situation of the tensile samples; (**b**) typical photograph of repaired sample and extra substrate plate.

In the repairing process, the substrates were 3 mm thick DZ411 superalloy plates, which were manufactured by directional solidification method and subjected to the standard heat treatment of 1225 °C 2 h/AC + 1120 °C 2 h/AC + 850 °C 24 h/AC. The IN738LC superalloy powder (the powder morphology is shown in Figure 2) was fed directly into the molten pool by a nozzle using coaxial powder feeding technology. After melting, it was deposited layer by layer on the substrates, with the depositing direction aligning with the solidification direction of the substrates. After the repairing process, samples were subjected to a post-repairing heat treatment of 1120 °C 2 h/AC + 850 °C 24 h/AC, which referred to the standard heat treatment of IN738LC [26]. To compare the mechanical properties between the deposit and substrate, extra substrate plates were also subjected to post-repairing heat treatment. The typical photograph of the repaired sample and extra substrate plate is shown in Figure 1b. No cracks were found in all the repaired samples.

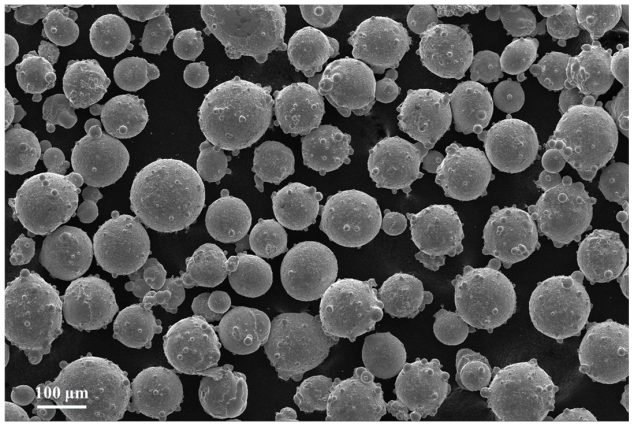

Figure 2. The morphology of IN738LC powder.

2.3. Microstructure Characterization and Tensile Test

To characterize the microstructure, the samples were polished and etched using an acid reagent (2.5 g $CuCl_2$, 50 mL HCl, and 50 mL H_2O). The microstructure of the repaired samples was characterized via optical microscopy (OM, LEICA-DM4000, Bruker, Billerica, MA, USA) and scanning electron microscopy (SEM, ZEISS-Gemini 300, ZEISS Group, Oberkochen, Germany).

In order to investigate the mechanical properties of each area of the repaired sample, tensile samples were taken from each area, with the main axis of the tensile sample being perpendicular to the depositing direction, as shown in Figure 1a. Tensile sample D is composed entirely of the IN738LC deposit; tensile sample S is composed entirely of DZ411 substrate; and tensile sample D + S is composed of both deposit and substrate. Three tensile tests were conducted on each type of tensile sample.

In addition, in order to analyze the changes in mechanical properties of local areas of the sample during the tensile test, the microhardness of the fractured samples was measured. The distribution of microhardness sampling points is depicted in Figure 3. These hardness values were compared to the undeformed repaired sample at the corresponding position to reflect the change in hardness between before and after the tensile test. An HAZ-1000 semiautomatic Viker tester was used for the microhardness test, and the test parameters were as follows: dwell time of 10 s and test load of 500 g.

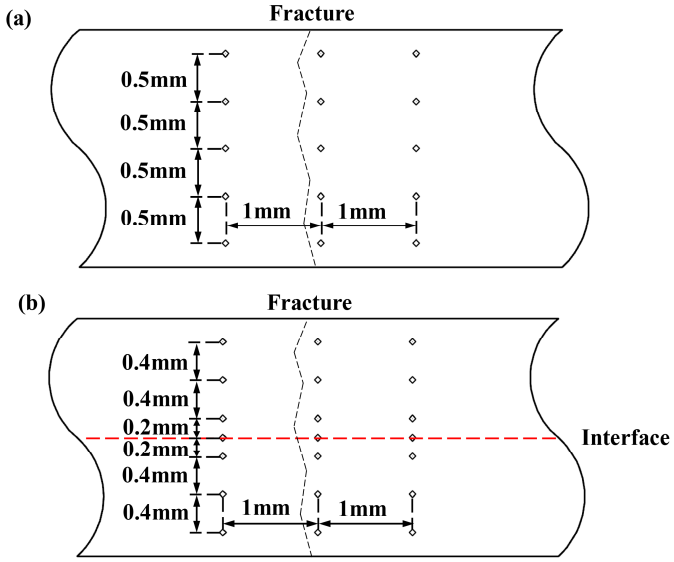

Figure 3. Schematic diagrams of the distribution of microhardness sampling points of (**a**) the tensile section of fractured D sample and S sample and (**b**) the tensile section of fractured D + S sample.

3. Results

3.1. Microstructure

The microstructure of the repaired sample is shown via OM and SEM in Figure 4. Apart from a tiny number of pores in the deposit, no additional visible defects were discovered in the repaired sample. The growth direction of the dendrites in the substrate stayed parallel to the solidification direction. Even though the dendritic width of the deposit was considerably lower than that of the substrate, most dendrite development directions were still inherited from the substrate. The refinement of dendrite width was a result of the quick cooling rate during the LMD process [8], and the consistency of growth direction was a result of the significant temperature gradient along the depositing direction during the LMD process [9]. A few equiaxed grains could also be observed near the interface, which might be formed by recrystallization.

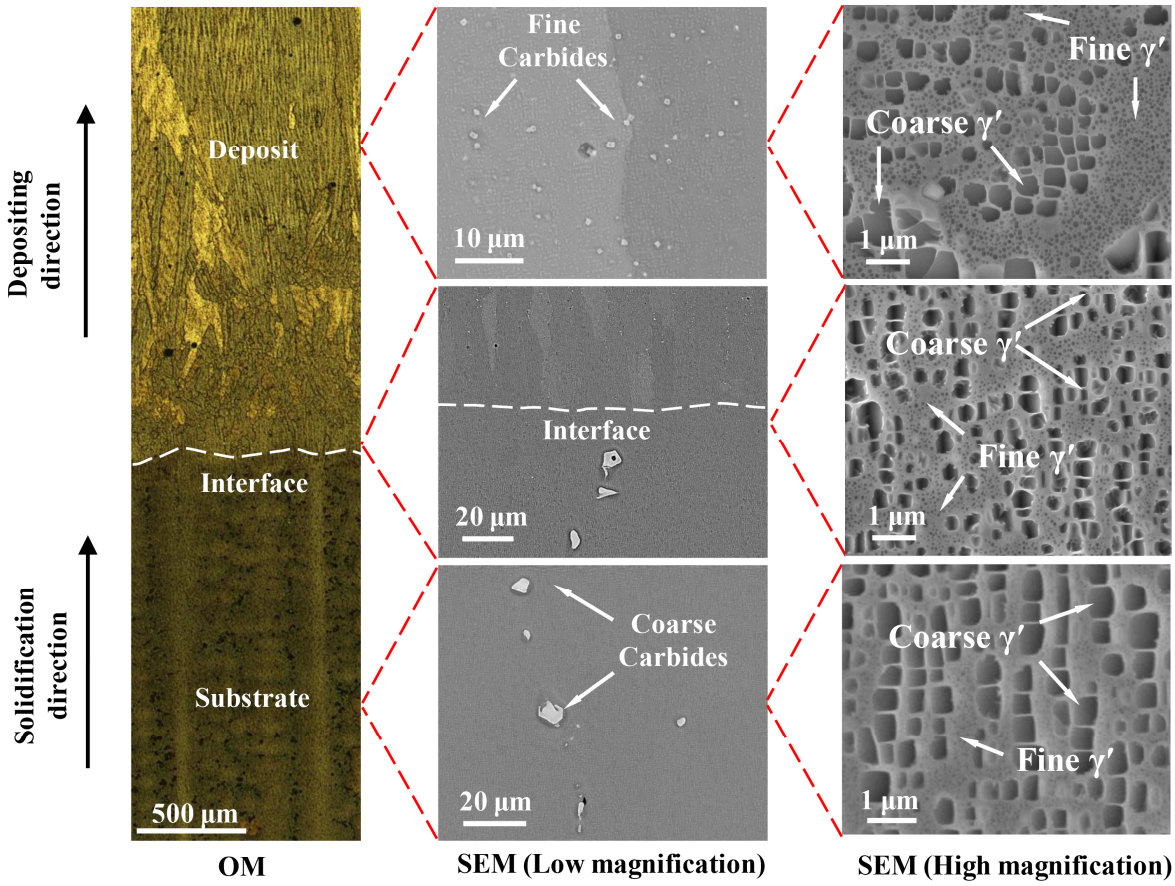

Figure 4. Microstructure of repaired sample.

The SEM images reveal that both the deposit and substrate exhibited a typical microstructure consisting of the γ phase as the matrix and the γ′ phase as the predominant strengthening phase [27,28]. All areas contained a small number of carbides, and no intermetallic compounds were found to be generated at the interface. Low-magnification SEM images demonstrate a considerable difference in carbide morphology among different areas. The carbides in the deposit and interface were primarily tiny and possessed either a round or square shape, with an average diameter of less than 0.5 μm. However, the carbides in the substrate were significantly coarser and had an irregular shape, with an average diameter of more than 4.0 μm. This discrepancy in the morphology of carbides between the two areas was due to the different cooling rates during the manufacturing process of the two areas [10]. Compared to the substrate, during the manufacturing process of the deposit, the cooling rate was faster, the degree of element segregation was lower, and the

morphology of the carbide was finer and more uniform. High-magnification SEM images reveal the bimodal shape of the γ' phase in each area of the repaired sample. The size of the fine γ' phase was comparable across all areas, measuring approximately 0.06 μm in diameter. The coarse γ' phase exhibited a consistent and progressive increase in size from the deposit to the substrate, with a side length of 0.28 μm in the deposit, a side length of 0.31 μm at the interface, and a side length of 0.38 μm in the substrate. According to Jackson and Reed [29], the coarse γ' phase was the phase that was not entirely dissolved in the solid solution treatment, whereas the fine γ' phase was the phase formed during the cooling process following the solid solution heat treatment. The substrate had undergone heat treatment before and after the repair procedure, so its coarse γ' phase had a longer growth time, resulting in a larger size and higher volume fraction of the coarse γ' phase [11].

3.2. Mechanical Properties

The stress–strain diagram and typical photograph of three types of tensile samples are shown in Figure 5. Due to the square shape of the tensile section of the samples, there was stress concentration at the corners of the sample. During the tensile testing, when the samples experienced pronounced localized plastic deformation, they might fracture rapidly from their corners. Hence, the sample photographs revealed a limited extent of plastic deformation, and the stress–strain curve for the period following necking was entirely absent.

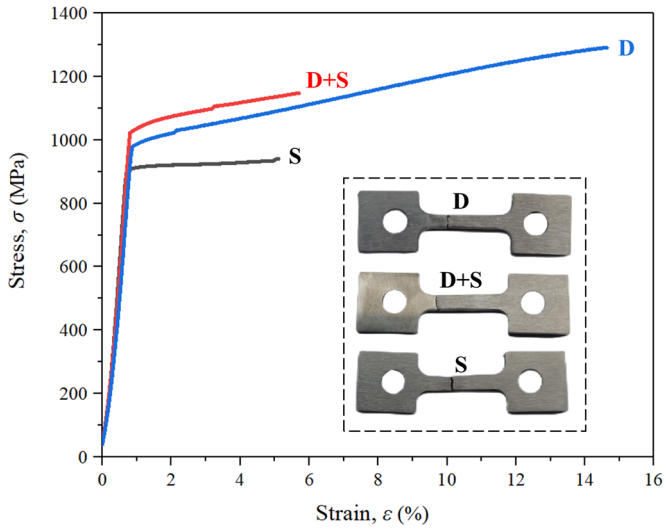

Figure 5. Stress–strain diagram and typical photograph of three types of tensile samples.

The tensile test results are shown in Table 3. In terms of ultimate tensile strength, it could be observed that D samples possessed the highest strength, while S samples possessed the lowest strength, with a notable disparity that exceeded 250 MPa between the two. The elongation values for both the S samples and the D + S samples were very similar, with both being about 6%. However, the D samples possessed an elongation value approximately twice as large as the previous two samples. The tensile test results indicated that the deposit had better mechanical properties than the substrate. Additionally, it could be noted that the D + S samples possessed the highest yield strength. According to the Hall–Petch relation [30], the large area grain boundary of fine equiaxed grains could hinder dislocation slip and increase the required driving force for dislocation slip, thus improving the yield strength of the alloy. Therefore, the high yield strength of the D + S samples might be attributed to the fine recrystallized equiaxed grains at the interface. Based on Table 3, it could also be found that the disparity in the ultimate tensile strength was much more significant than the disparity in the yield strength among the three types of samples. This indicated that the three types of samples exhibited a considerable difference in the

work-hardening effect. The work-hardening effect of the D sample was the best, followed by that of the D + S samples, and that of the S samples was the worst.

Table 3. Tensile test results of three types of tensile samples.

Samples	Ultimate Tensile Strength (MPa)	Yield Strength (MPa)	Elongation (%)
D	942 ± 6	905 ± 11	5.8 ± 0.3
D + S	1102 ± 55	986 ± 40	6.0 ± 0.7
S	1240 ± 45	957 ± 37	10.7 ± 2.0

Figure 6 demonstrates the change in average hardness values of samples before and after the tensile test. The hardness values of the interface and the 0.2 mm area near the interface in the D + S sample are considered as the hardness of the interface. The hardness values of the remaining sampling points are defined as the hardness values of the deposit and the substrate in the D + S sample. Before the tensile test, it was seen that the hardness at the interface exhibited the lowest value, mostly because the recrystallized grains near the interface released internal stress, hence decreasing their hardness values. After being away from the recrystallization position, the hardness values increased. After the tensile test, the hardness values of all the samples increased, and there was a significant disparity in the hardness increment between different samples. Furthermore, the disparity in the hardness increment for each sample surpassed the disparity in hardness before the tensile test, indicating the disparity in hardness increment as the determining factor for the disparity in hardness after the tensile test. The observed increase in hardness could be attributed to the work-hardening effect of the samples, and the increment in hardness could serve as an indicator of the work-hardening effect [31]. In Figure 6, the hardness values of the D sample before the tensile test were comparable to those of the S sample, but the hardness increment of the D sample was greater than that of the S sample, resulting in the D sample having a higher hardness value than the S sample. This demonstrated that the work-hardening effect of the D sample was superior to that of the S sample, which was consistent with the analysis of the tensile test result. In the D + S sample, the deformation degree of each region was identical, and the hardness increment of the deposit was greater than that of the substrate, indicating that the work-hardening efficiency of the deposit was greater than that of the substrate. It was worth noting that the hardness of the interface in the D + S sample also increased greatly, indicating that the work-hardening efficiency of the interface was also high. Due to the high work-hardening efficiency of the deposit and interface in the D + S sample, the D + S sample could have a higher hardness value than the S sample under a similar degree of plastic deformation.

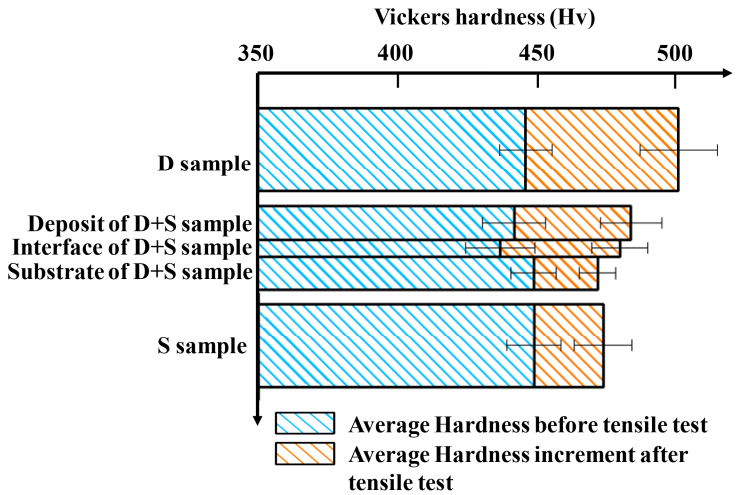

Figure 6. The change in average hardness of D sample, D + S sample, and S sample.

4. Discussion

The fractography of the three types of tensile samples is used to aid in the analysis of the mechanical property differences among the three, as shown in Figure 7. The fracture morphology of the S sample revealed that the S sample fracture mode was a brittle fracture mode that cracks along the grain boundary. On the fracture surface, there were numerous holes created by the carbide separated from the grain boundary, and under magnification, the remaining broken carbide could be observed. This phenomenon demonstrated that the coarse and irregularly shaped carbides in the S sample might result in mechanical property deterioration in the grain boundary. During the tensile test, micropores might develop at the boundary of these carbides, or generate from the directly broken carbides, which grew and finally linked to form cracks [32]. These cracks resulted in the rapid fracture of the S sample, which was the reason for the low relative elongation of the S sample.

The fracture morphology of the D sample indicated that it had a mixed fracture mode (Figure 7b). On the fracture surface of the D sample, two morphologies could be observed. One was a grain boundary cracking surface similar to that of the S sample but with a considerably smaller area, which might be attributable to the reduced grain size of the D sample. The other fracture morphology was a typical equiaxed dimple fracture, with tiny carbide particles in the middle of the equiaxed dimples. The size of carbides in the D sample was significantly smaller than that in the S sample, and the shape was more regular, resulting in less deterioration of the mechanical properties of the D sample. Hence, the superior ductility of the D sample might be a result of its fine grain and fine, uniform carbides.

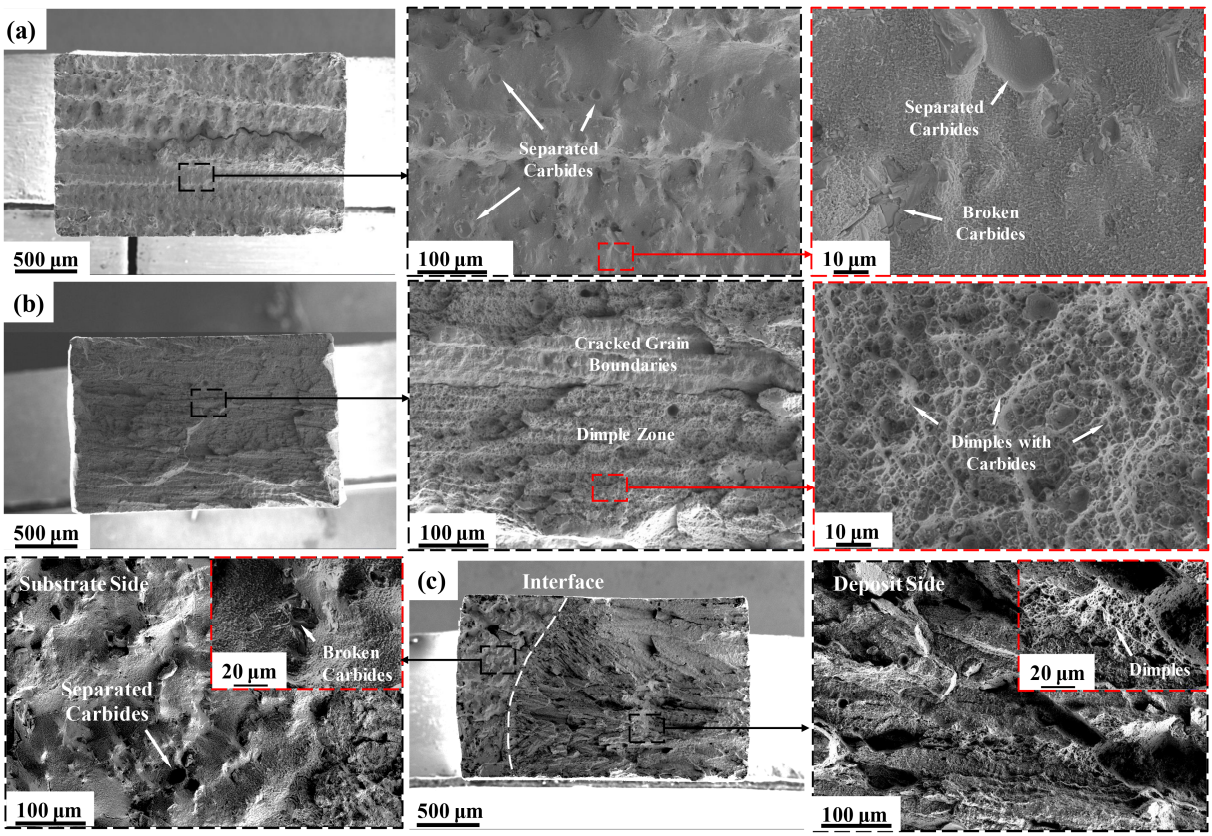

Figure 7. Fractography of three types of tensile samples: (**a**) S sample, (**b**) D sample, and (**c**) D + S sample.

The D + S sample had a more complicated fracture morphology. As shown in Figure 7c, the fracture of the D + S sample had two morphologies, which were found on the substrate side and the deposit side, respectively. The interface could clearly separate the two morphologies. The morphology of the substrate side was quite similar to that of the S sample, both of which were cracks along grain boundaries, and there were holes left by separated carbides and broken carbides on the surface. On the deposit side, a great number of tearing edges formed from the interface were spread, and there were still some dimples on the surface of the tearing edges. This morphology showed that the crack initiation of the D + S sample was similar to that of the S sample, that is, the cracks formed by the broken coarse carbides or the separation of carbides from the matrix. Therefore, D + S samples and S samples exhibited similar relative elongation.

The work-hardening effect of alloys is related to the density of geometrically necessary dislocations (GNDs) generated during plastic deformation [33]. EBSD kernel average misorientation (KAM) maps can illustrate the distribution of the density of GNDs in alloys. In the KAM map, the KAM values represent the local misorientation, which has a positive correlation with the density of GNDs [34]. Figure 8 shows the KAM maps of the three types of fractured samples near the fractured surface, and the thin white solid lines in Figure 8 represent the grain boundaries identified by the software. Figure 8a shows that the fractured D sample had the highest density of GNDs. This phenomenon might be attributed to the largest plastic deformation experienced by the D sample, leading to the generation of a large number of GNDs. In Figure 8b, for the D + S sample, the interface and nearby recrystallized grains (RG) had the highest KAM value. Due to the inconsistent mechanical properties of the deposit and the substrate in the D + S sample, there was a maximum strain gradient at the interface during the deformation of the D + S sample, promoting the generation of GNDs [35]. In addition, the grain size of the RG at the interface was very small, hence inhibiting the dislocation slip efficiently and hindering the dislocation annihilation during the plastic deformation process. Therefore, the interface and nearby RG had the maximal density of GNDs in the D + S sample after the tensile test, improving the hardness of the interface and its surrounding positions. It can also be noted that the deposit in the D + S sample had a higher density of GNDs than the substrate in the D + S sample, which might be because the microstructure of the deposit in the D + S sample was more refined than the substrate in the D + S sample. In Figure 8c, dislocations were primarily concentrated near carbides in the S sample. This phenomenon demonstrated that the carbides in the S sample had the ability to inhibit dislocation slipping. However, due to their large size and irregular shape, these carbides were prone to breaking, and their adhesion to the metal matrix was poor. When dislocations piled up at the boundary of these carbides, the carbides might directly break or separate from the matrix, which led to rapid fracture. Therefore, the diminished mechanical properties of the S sample could be attributed to the coarse carbides in the sample.

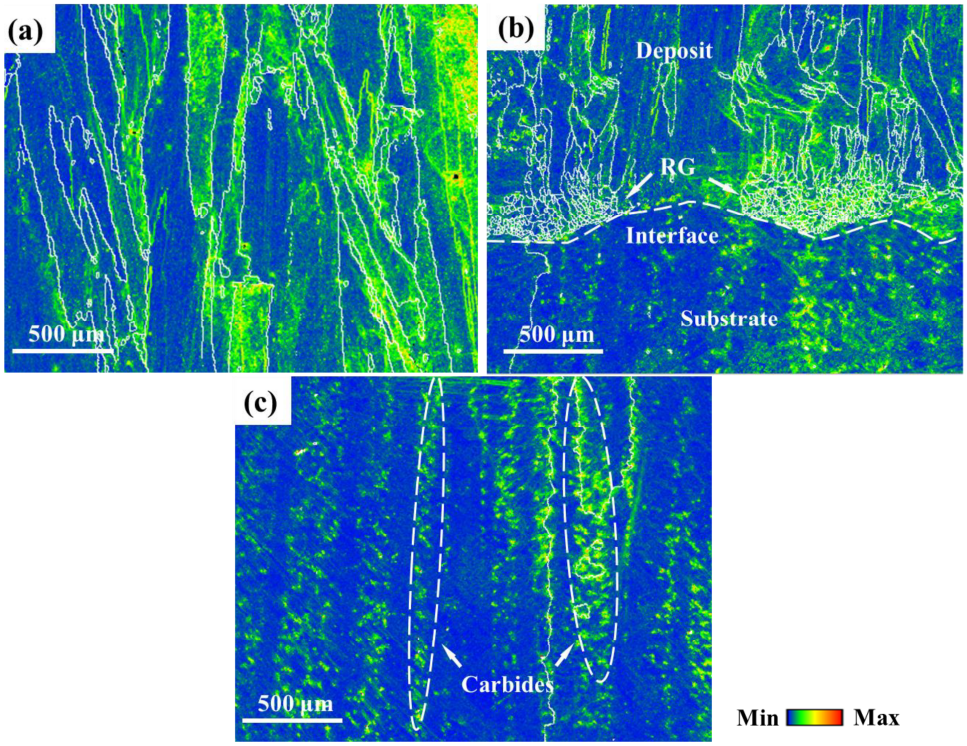

Figure 8. The KAM maps of (**a**) fractured D sample, (**b**) fractured D + S sample, and (**c**) fractured S sample.

5. Conclusions

Using an LMD-based repairing technique, crack-free repair samples with γ' phase precipitation-strengthened Ni-based superalloy DZ411 as substrate and IN738LC alloy as deposit were manufactured. The microstructure of the repaired samples was characterized, and the mechanical properties were measured. The main conclusions are as follows:

(1) Owing to the rapid cooling rate and high-temperature gradient during the LMD process, the microstructure in the deposit was evidently refined compared to that in the substrate, and the growth direction of the dendrite could be approximately consistent with the substrate.

(2) The S samples exhibited poor mechanical properties, as demonstrated by its ultimate tensile strength of 942 MPa and relative elongation of 5.8%. The reason for this is that large-sized carbides were prone to breaking, and their adhesion to the metal matrix was poor, which caused the S samples to fracture rapidly during the tensile test.

(3) Among the three types of samples, the D samples had the greatest mechanical properties, with an ultimate tensile strength of 1240 MPa and a relative elongation of 10.7%. These fine microstructures in the IN738LC deposit enhanced the ductility of the alloy, enabling it to generate more GNDs during the larger plastic deformation process, thereby strengthening the alloy.

(4) The crack initiation mechanism in the D + S sample exhibited similarity to that of the S sample, so the relative elongation of the two samples was equivalent, both below 6%. However, due to the greater work-hardening efficiency exhibited by the interface and deposit of the D + S sample, the D + S sample had greater strength and hardness after the tensile test than the S sample.

The research results show that using an LMD-based repairing technique with IN738LC superalloy to repair γ' phase precipitation-strengthened Ni-based superalloy DZ411 is a feasible solution and can provide some references for future research.

Author Contributions: W.Y.—Conceptualization, Investigation, Writing—original draft; B.X.—Data curation, Validation; J.L.—Validation; M.Z.—Investigation; X.B.—Conceptualization, Methodology, Writing—review and editing. All authors have read and agreed to the published version of the manuscript.

Funding: The work was financially supported by the National Science and Technology Major Project (J2019-IV-0006-0074).

Institutional Review Board Statement: Not applicable.

Informed Consent Statement: Not applicable.

Data Availability Statement: The data that support the findings of this study are available from the corresponding author, Xiang-de Bian, upon reasonable request.

Conflicts of Interest: The authors declare no conflict of interest.

References

1. Xu, R.; Li, Y.; Yu, H. Creep Behavior and Deformation Mechanism of a Third-Generation Single Crystal Ni-Based Superalloy at 980 °C. *Metals* **2023**, *13*, 1541. [CrossRef]
2. Yan, W.-G.; Zeng, W.; Man, J.-X.; Qiao, D.; Zhang, Z.-X.; Bian, X.-D. Microstructure and mechanical properties of a directionally solidified superalloy DZ411 plate sample repaired by laser melting deposition. *Mater. Sci. Eng. A* **2023**, *876*, 145141. [CrossRef]
3. Chen, J.; Chen, J.; Wang, Q.; Wu, Y.; Li, Q.; Xiao, C.; Hui, X. Mutation in TCP phases and superior stress rupture life led by W/Mo ratio in Ni-based single crystal superalloys. *Mater. Lett.* **2022**, *312*, 131656. [CrossRef]
4. Yang, Q.; Xu, Z.; Li, L.; Li, P. Microstructure and Performance Research on Ceramic-Enhanced Inconel 718 Matrix Composite Using Laser Additive Manufacturing. *Metals* **2023**, *13*, 1525. [CrossRef]
5. Wang, J.; Pan, Z.; Wang, Y.; Wang, L.; Su, L.; Cuiuri, D.; Zhao, Y.; Li, H. Evolution of crystallographic orientation, precipitation, phase transformation and mechanical properties realized by enhancing deposition current for dual-wire arc additive manufactured Ni-rich NiTi alloy. *Addit. Manuf.* **2020**, *34*, 101240. [CrossRef]
6. Li, L.; Deceuster, A.; Zhang, C. Effect of Process Parameters on Pulsed-Laser Repair of a Directionally Solidified Superalloy. *Met. Microstruct. Anal.* **2012**, *1*, 92–98. [CrossRef]
7. Moattari, M.; Shokrieh, M.M.; Moshayedi, H.; Kazempour-Liasi, H. Evaluations of residual stresses in repair welding of Ni-based IN939 superalloy. *J. Therm. Stress.* **2020**, *43*, 801–815. [CrossRef]
8. Rush, M.T.; Colegrove, P.A.; Zhang, Z.; Broad, D. Liquation and post-weld heat treatment cracking in Rene 80 laser repair welds. *J. Mater. Process. Technol.* **2012**, *212*, 188–197. [CrossRef]
9. Liu, G.; Du, D.; Wang, K.; Pu, Z.; Chang, B. Hot cracking behavior and mechanism of the IC10 directionally solidified superalloy during laser re-melting. *Vacuum* **2020**, *181*, 109563. [CrossRef]
10. Bidron, G.; Doghri, A.; Malot, T.; Fournier-Dit-Chabert, F.; Thomas, M.; Peyre, P. Reduction of the hot cracking sensitivity of CM-247LC superalloy processed by laser cladding using induction preheating. *J. Mater. Process. Technol.* **2019**, *277*, 116461. [CrossRef]
11. Griffiths, S.; Tabasi, H.G.; Ivas, T.; Maeder, X.; De Luca, A.; Zweiacker, K.; Wróbel, R.; Jhabvala, J.; Logé, R.; Leinenbach, C. Combining alloy and process modification for micro-crack mitigation in an additively manufactured Ni-base superalloy. *Addit. Manuf.* **2020**, *36*, 101443. [CrossRef]
12. Guo, C.; Li, G.; Li, S.; Hu, X.; Lu, H.; Li, X.; Xu, Z.; Chen, Y.; Li, Q.; Lu, J.; et al. Additive manufacturing of Ni-based superalloys: Residual stress, mechanisms of crack formation and strategies for crack inhibition. *Nano Mater. Sci.* **2023**, *5*, 53–77. [CrossRef]
13. Xu, J.; Ding, Y.; Gao, Y.; Wang, H.; Hu, Y.; Zhang, D. Grain refinement and crack inhibition of hard-to-weld Inconel 738 alloy by altering the scanning strategy during selective laser melting. *Mater. Des.* **2021**, *209*, 109940. [CrossRef]
14. Guo, C.; Zhou, Y.; Li, X.; Hu, X.; Xu, Z.; Dong, E.; Zhu, Q.; Ward, R.M. A comparing study of defect generation in IN738LC superalloy fabricated by laser powder bed fusion: Continuous-wave mode versus pulsed-wave mode. *J. Mater. Sci. Technol.* **2021**, *90*, 45–57. [CrossRef]
15. Carpenter, K.; Tabei, A. On Residual Stress Development, Prevention, and Compensation in Metal Additive Manufacturing. *Materials* **2020**, *13*, 255. [CrossRef]
16. Xu, J.; Lin, X.; Guo, P.; Yang, H.; Xue, L.; Huang, W. The microstructure evolution and strengthening mechanism of a γ'-strengthening superalloy prepared by induction-assisted laser solid forming. *J. Alloys Compd.* **2019**, *780*, 461–475. [CrossRef]
17. Yu, Z.; Guo, C.; Han, S.; Hu, X.; Cao, L.; Xu, Z.; Ding, H.; Zhu, Q. The effect of Hf on solidification cracking inhibition of IN738LC processed by Selective Laser Melting. *Mater. Sci. Eng. A* **2021**, *804*, 140733. [CrossRef]
18. Ci, S.; Liang, J.; Li, J.; Zhou, Y.; Sun, X. Microstructure and tensile properties of DD32 single crystal Ni-base superalloy repaired by laser metal forming. *J. Mater. Sci. Technol.* **2020**, *45*, 23–34. [CrossRef]
19. Fang, X.; Li, Z.; Wang, Y.; Ruiz, M.; Ma, X.; Wang, H.; Schoell, R.; Zheng, C.; Kaoumi, D.; Zhu, Y. Achieving high hetero-deformation induced (HDI) strengthening and hardening in brass by dual heterostructures. *J. Mater. Sci. Technol.* **2021**, *98*, 244–247. [CrossRef]

20. Wu, X.; Zhu, Y.; Lu, K. Ductility and strain hardening in gradient and lamellar structured materials. *Scr. Mater.* **2020**, *186*, 321–325. [CrossRef]
21. Tan, X.; Kok, Y.; Tan, Y.J.; Descoins, M.; Mangelinck, D.; Tor, S.B.; Leong, K.F.; Chua, C.K. Graded microstructure and mechanical properties of additive manufactured Ti–6Al–4V via electron beam melting. *Acta Mater.* **2015**, *97*, 1–16. [CrossRef]
22. Yuhua, C.; Yuqing, M.; Weiwei, L.; Peng, H. Investigation of welding crack in micro laser welded NiTiNb shape memory alloy and Ti6Al4V alloy dissimilar metals joints. *Opt. Laser Technol.* **2017**, *91*, 197–202. [CrossRef]
23. Chen, Y.; Yao, Z.; Dong, J.; Zhao, W.; Xiao, H.; Chen, X. Molecular dynamics simulation of the γ' phase deformation behaviour in nickel-based superalloys. *Mater. Sci. Technol.* **2022**, *38*, 1439–1450. [CrossRef]
24. Peng, P.; Lu, L.; Liu, Z.; Pei, X.; Gan, L.; Xu, Y.; Zhang, X.; Ma, Z.; Guo, M.; Liu, L. Investigation on the influence of Ta on the micro-structure evolution of Ni-based superalloy DZ411 during directional solidification, heat treatment, and long-term aging. *J. Alloys Compd.* **2022**, *920*, 165886. [CrossRef]
25. Academic Committee of the Superalloys CSM. *China Superalloys Handbook*; Standards Press of China: Beijing, China, 2012.
26. Xu, J.; Gruber, H.; Boyd, R.; Jiang, S.; Peng, R.L.; Moverare, J.J. On the strengthening and embrittlement mechanisms of an additively manufactured Nickel-base superalloy. *Materialia* **2020**, *10*, 100657. [CrossRef]
27. Holländer, D.; Kulawinski, D.; Thiele, M.; Damm, C.; Henkel, S.; Biermann, H.; Gampe, U. Investigation of isothermal and ther-mo-mechanical fatigue behavior of the nickel-base superalloy IN738LC using standardized and advanced test methods. *Mater. Sci. Eng. A* **2016**, *670*, 314–324. [CrossRef]
28. Wu, Y.; Chen, J.; Zhang, L.; Ji, J.; Wang, Q.; Zhang, S. Effect of boron on the structural stability, mechanical properties, and electronic structures of γ'-Ni3Al in TLP joints of nickel-based single-crystal alloys. *Mater. Today Commun.* **2022**, *31*, 103375. [CrossRef]
29. Jackson, M.; Reed, R. Heat treatment of UDIMET 720Li: The effect of microstructure on properties. *Mater. Sci. Eng. A* **1999**, *259*, 85–97. [CrossRef]
30. Guo, B.; Zhang, Y.; He, F.; Ma, J.; Li, J.; Wang, Z.; Wang, J.; Feng, J.; Wang, W.; Gao, L. Origins of the mechanical property heterogeneity in a hybrid additive manufactured Hastelloy X. *Mater. Sci. Eng. A* **2021**, *823*, 141716. [CrossRef]
31. Movahed, P.; Kolahgar, S.; Marashi, S.; Pouranvari, M.; Parvin, N. The effect of intercritical heat treatment temperature on the tensile properties and work hardening behavior of ferrite–martensite dual phase steel sheets. *Mater. Sci. Eng. A* **2009**, *518*, 1–6. [CrossRef]
32. Li, J.; Wang, H. Microstructure and mechanical properties of rapid directionally solidified Ni-base superalloy Rene'41 by laser melting deposition manufacturing. *Mater. Sci. Eng. A* **2010**, *527*, 4823–4829. [CrossRef]
33. Zhang, S.; Lin, X.; Wang, L.; Yu, X.; Hu, Y.; Yang, H.; Lei, L.; Huang, W. Strengthening mechanisms in selective laser-melted Inconel718 superalloy. *Mater. Sci. Eng. A* **2021**, *812*, 141145. [CrossRef]
34. Yan, Z.; Wang, D.; He, X.; Wang, W.; Zhang, H.; Dong, P.; Li, C.; Li, Y.; Zhou, J.; Liu, Z.; et al. Deformation behaviors and cyclic strength assessment of AZ31B magnesium alloy based on steady ratcheting effect. *Mater. Sci. Eng. A* **2018**, *723*, 212–220. [CrossRef]
35. Li, X.; Lu, L.; Li, J.; Zhang, X.; Gao, H. Mechanical properties and deformation mechanisms of gradient nanostructured metals and alloys. *Nat. Rev. Mater.* **2020**, *5*, 706–723. [CrossRef]